A novel approach to model fretting-fatigue in multiaxial and non-proportional loading conditions

Guillaume Rousseau, Claudio Montebello, Yoann Guilhem, Sylvie Pommier

A novel approach to model fretting fatigue in multiaxial and non-proportional loading conditions

Guillaume Rousseau[a,b,*], Claudio Montebello[b], Yoann Guilhem[a], Sylvie Pommier[a]

[a] *Laboratoire de Mécanique et Technologie (LMT), ENS Paris–Saclay/CNRS/Université Paris–Saclay, 61 avenue du Président Wilson, 94235 Cachan, France*
[b] *Safran Aircraft Engines*

Abstract

This approach consists of representing the movement in the vicinity of a contact front by using a set of degrees of freedom and reference spatial fields. The latter are built, once and for all, by a principal component analysis of the velocity field (Karhunen-Loeve transform) and are hence tailored to provide the best possible approximation of the velocity field close to the contact front. The intensity factors of these reference spatial fields are hence a set of non-local variables which constitute the degrees of freedom of the problem. It is shown that a very small number of them is required to accurately describe the mechanical problem. The so-called "linear intensity factors" $\underline{I}$ characterize the elastic part of the field while the "complementary intensity factors" $\underline{I}^c$ characterize partial slip within the contact area. 3D finite element analyses were conducted, first to build the framework of this approximation, second to qualify its accuracy and finally to determine the non-linear response of a contact in multiaxial fretting-fatigue conditions. Finally an incremental constitutive model was developed to predict this non-linear response and was compared to the results of the finite elements analyses. This non-local representation has the advantage of being independent of the geometry of the contacting bodies. So, intensity factors can be used to predict the behavior of real-scale industrial assembly using data obtained on laboratory test geometry.

Keywords: Fretting-fatigue, Crack analogue, Size effect

1. Introduction

Fretting-fatigue occurs in engineering assemblies subjected to vibration loads. Micro-slip caused by oscillating forces, between the contacting bodies, leads to surface damage, crack initiation and growth in fretting. Combined with bulk fatigue loading, crack propagation up to fracture may occur. Consequently, fretting-fatigue is a major concern in safety-critical industries such as aerospace [14]. Experimental test campaigns have shown that this phenomenon has a significant detrimental effect on the material fatigue limit [10] by initiating embryo cracks very early in life. One of the major difficulties in dealing with the fretting fatigue problem is the severe stress gradient below the contact surface in the vicinity of the contact edge. Local approaches used to predict the fatigue life based on the stresses at the hot spots are over-conservative for fretting-fatigue because they do not account for the possibility of crack arrest due to a strong stress gradient from the surface to the bulk. Moreover, the crack initiation threshold is not unique in terms of local quantities (Fig. 1) and shows a strong dependency to the geometry [4, 6]. However, using the Theory of critical distance [18], it is possible to predict crack arrest and consequently to estimate fretting fatigue life and the gradient effect with a good degree of accuracy [2, 4–6, 17].

In spite of the good predictions of fretting-fatigue threshold obtained using the Theory of critical distance, there are criticisms with respect to the use of critical length as a material property [3]. Thus, the transferability of results obtained on laboratory samples (cylinder-plane contact) to industrial cases (disk-blade interface), which are complex and 3D geometry, is not guaranteed.

To overcome this problem, a non-local modeling

*Corresponding author.

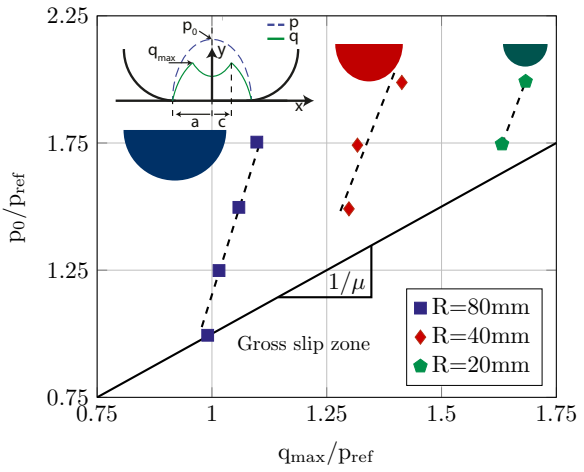

Figure 1: Experimental crack initiation boundary for Inconel 718 in plain fretting [1].

will be used. The model proposed hereunder is an extension of the 2D modeling set up by Montebello [12]. This approach is based on two main ideas: (i) a similarity between the mechanical fields induced by the severe stress gradient extremely localized at the edge of the contact in fretting-fatigue and the ones present around a crack or a notch [7–9]; (ii) an original approach to describe mixed-mode cyclic elastic-plastic behavior reasonably precise near the crack tip using a set of condensed variables [15, 16].

The goal of this paper is to propose a solution to predict the velocity field close to the contact edge, and it will be divided into three major parts.

In the first section, the description of the velocity field through non-local intensity factors originally made by Montebello [13] is developed and extended in 3D to take into account complex and non-proportional tangential loading. In the second part, a model, proposed through an incremental formulation in order to use it with complex loading, to predict precisely the velocity field close to the contact edge is presented. In the last part, the influence of the Coulomb friction coefficient on the incremental model is studied.

2. Modeling

2.1. Background

The interest of this approach is shown in Fig. 2 where the description of crack initiation boundaries through non-local intensity factors shows a unique threshold. Hence, the geometry and consequently the gradient have no effect on these variables.

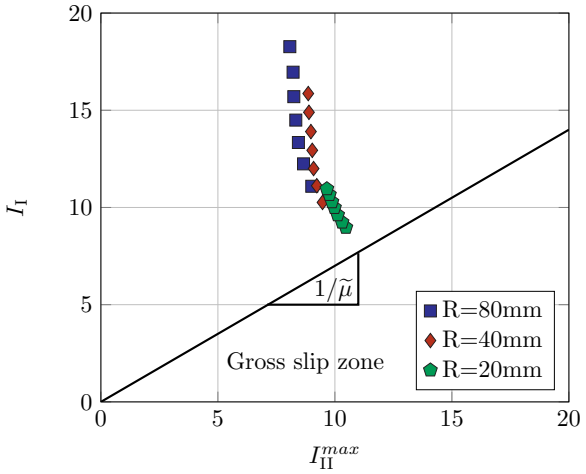

Figure 2: Non-local crack initiation boundary for Inconel 718 in plain fretting [13].

In this part, the computation of the reference fields and the associated intensity factors on a 3D geometry (Fig. 3) will be explained.

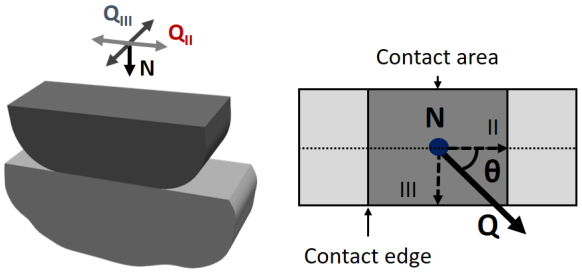

Figure 3: Fretting-fatigue model.

2.2. Mechanical field partitioning

As cracks initiation under fretting fatigue loading condition is located in the slip zone due to a high shear stress close to the contact edge, a fine mesh (5 to 10 µm) is required to capture the velocity field with a relevant precision . To overcome this time-consuming problem, the idea is to describe the velocity field close to the contact edge (Fig. 4) through a set of condensed variables.

Analogous to fracture mechanics, a local self-similar geometry and a strong stress gradient makes the spatial distribution of the mechanic fields imposed by the geometry while its intensity is determined by the macroscopic loads. Consequently, the

field, in the coordinate system R' attached to the contact edge (see Fig. 4) where P is the position coordinates vector, I_{I} ,I_{II} and I_{III} the elastic intensity factors, I^c_{II} and I^c_{III} the complementary intensity factors and ϕ_{I}, ϕ_{II}, ϕ_{III}, ϕ^c_{II} and ϕ^c_{III} the associated reference fields, can be expressed through a sum of products between an intensity factor (time dependent) and a reference field (geometry dependent) :

$$\underline{v}(\underline{P},t)_{R'} \simeq \underbrace{\dot{I}_I(t)\underline{\phi}_I(\underline{P}) + \dot{I}_{\mathrm{II}}(t)\underline{\phi}_{\mathrm{II}}(\underline{P}) + \dot{I}_{\mathrm{III}}(t)\underline{\phi}_{\mathrm{III}}(\underline{P})}_{\underline{v}_e} + \underbrace{\dot{I}^c_{\mathrm{II}}(t)\underline{\phi}^c_{\mathrm{II}}(\underline{P}) + \dot{I}^c_{\mathrm{III}}(t)\underline{\phi}^c_{\mathrm{III}}(\underline{P})}_{\underline{v}_c} \quad (1)$$

The field is partitioned into two terms: the elastic one $\underline{v}_e$ represents the linear elastic response of the structure; the complementary one $\underline{v}_c$ describes the non-linear contribution due to friction in the slip zone. In turn, $\underline{v}_e$ is separated into a symmetric, antisymmetric and anti-planar part with respect to the contact plane and $\underline{v}_c$ is only separated into a antisymmetric and anti-planar part.

The partition is done on the velocity field rather than on the stress or displacement fields because the velocity is an extensive variable that allows to properly characterize the non-linear contribution of the friction. The intensity factors represent the degrees of freedom of our approximated problem while the reference fields form an orthonormal basis which allows to describe quite well the problem with few variables.

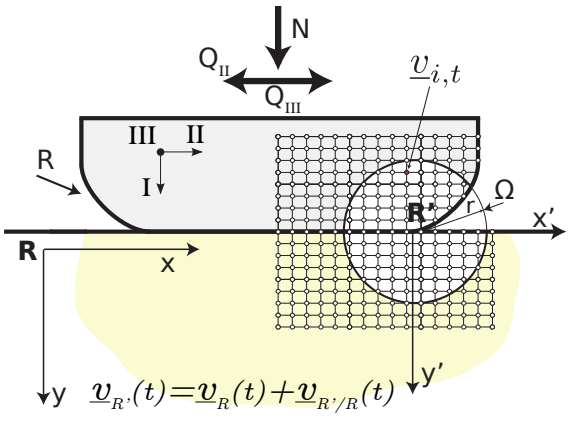

Figure 4: Extraction area.

2.3. FE computation and post-processing

The FE simulation consists of an elastic quasi-static computation performed by ABAQUS. To model the contact, the Lagrange multipliers technique is chosen with a friction Coulomb law. Close to the contact, a regular mesh with linear elastic hexahedron elements is employed. The maximum length of these elements is 20 μm in order to ensure short computational time and a quite good convergence with the analytical solution. Concerning the loadings (Fig. 3), a constant normal load N and cyclic tangential loads Q_{II} and Q_{III} are applied at the top of the pad to simulate fretting cycles.

The velocity field is obtained for each mesh node and for all the simulation time step. However the post-processing will be applied only in a circular region Ω centered at the contact edge and in the median plan of the geometry (Fig. 4).

With the crack analog hypothesis, the velocity field at the contact edge is considered to be comparable to the one at the crack tip.

To perform the partitioning of the linear velocity field (Eq. 2), the symmetric, antisymmetric and anti-planar reference fields, analogous respectively to mode I, mode II and mode III in LEFM, are generated respectively by a variation of normal (N) and tangential (Q_{II}, Q_{III}) forces. Moreover, to separate the elastic response from the non-linear contribution of the friction arising in the slip zone, the linear field (ϕ_*) are determined during a situation where all the contact surface is stuck.

$$\underline{v}_e(\underline{P},t) \simeq \dot{I}_I(t)\underline{\phi}_I(\underline{P}) + \dot{I}_{\mathrm{II}}(t)\underline{\phi}_{\mathrm{II}}(\underline{P}) + \dot{I}_{\mathrm{III}}(t)\underline{\phi}_{\mathrm{III}}(\underline{P}) \quad (2)$$

The Karhunen-Loeve decomposition [11] is applied to separate the radial and angular dependence of the reference fields.

$$\underline{\phi}_*(\underline{P}) \rightarrow \underline{\phi}_*(r,\theta) = f_*(r)\underline{g}_*(\theta) \quad (3)$$

The comparison (Fig. 5-6) between the analytic solution from LEFM [19] for mode III (Eq. 4) and the anti-planar reference field computed show a good correlation and validate the crack tip analogy.

$$u_{\mathrm{IIIz}} = \underbrace{K_{\mathrm{III}}}_{I_{\mathrm{III}}} \quad \underbrace{\frac{4(1+\nu)}{E}\sqrt{\frac{r}{2\pi}}}_{f(r)} \quad \underbrace{\left(-\cos\left(\frac{\theta}{2}\right)\right)}_{g(\theta)} \quad (4)$$

The intensity factors are computed by projecting the velocity field $\underline{v}$ to the reference field $\underline{\phi}_*$:

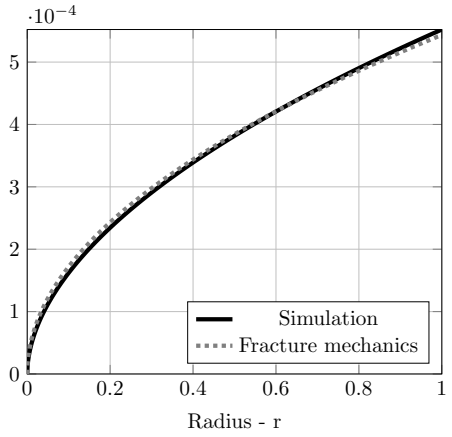

Figure 5: Comparison between radial evolution of ϕ_{III} and the displacement field at the crack tip (Mode III).

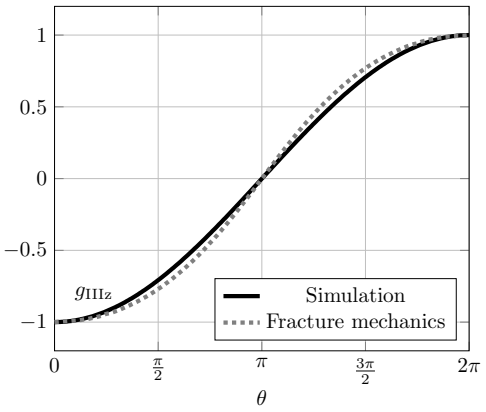

Figure 6: Comparison between angular evolution of ϕ_{III} and the displacement field at the crack tip (Mode III).

$$\dot{I}_*(t) = \frac{\int_\Omega \underline{v} \cdot \underline{\phi}_*}{\int_\Omega \underline{\phi}_* \cdot \underline{\phi}_*} \tag{5}$$

The Karhunen-Loeve decomposition is performed once again on the complementary field (Eq.6) to separate the field in a sum of two products (one for each tangential direction) between two functions depending separately on time and space (Eq.7).

$$\underline{v}_c(\underline{P},t) = \underline{v}(\underline{P},t) - \underline{v}_e(\underline{P},t) \tag{6}$$

$$\underline{v}_c(\underline{P},t) \simeq \dot{I}^c_{\mathrm{II}}(t)\underline{\phi}^c_{\mathrm{II}}(\underline{P}) + \dot{I}^c_{\mathrm{III}}(t)\underline{\phi}^c_{\mathrm{III}}(\underline{P}) \tag{7}$$

The radial evolution of ϕ^c_{III} (Fig. 7) show an exponential decrease which get along with the self-similar geometry hypothesis and confirms the very localized effect of the friction in the partial slip regime. The discontinuity due to the slip is shown in Fig. 8 by a displacement discontinuity between the two faces of the contact ($\theta = 0$ and $\theta = 2\pi$).

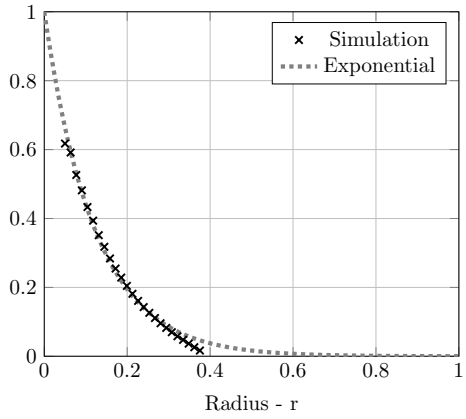

Figure 7: Radial evolution of ϕ^c_{III}.

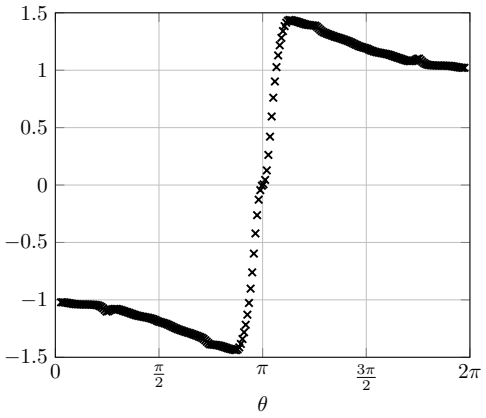

Figure 8: Angular evolution of ϕ^c_{III}.

2.4. Quality of the assumption

Once the reference fields and the intensity factors are identified, the final approximation of the velocity field is obtained (Eq. 1) and the elastic (Eq. 8) and total (Eq. 9) errors of the approximation are defined.

$$\xi_{el} = \frac{\sqrt{\int_\Omega (\underline{v} - \underline{v}_e)^2}}{\sqrt{\int_\Omega (\underline{v})^2}} \tag{8}$$

$$\xi_{tot} = \frac{\sqrt{\int_\Omega (\underline{v} - \underline{v}_e - \underline{v}_c)^2}}{\sqrt{\int_\Omega (\underline{v})^2}} \tag{9}$$

The error evolution during a proportional fretting cycle (Fig. 9) show the elastic error is low only when all the contact is stuck. However, with the introduction of the non-linear terms in the approximation, the error remains low during the whole cycle.

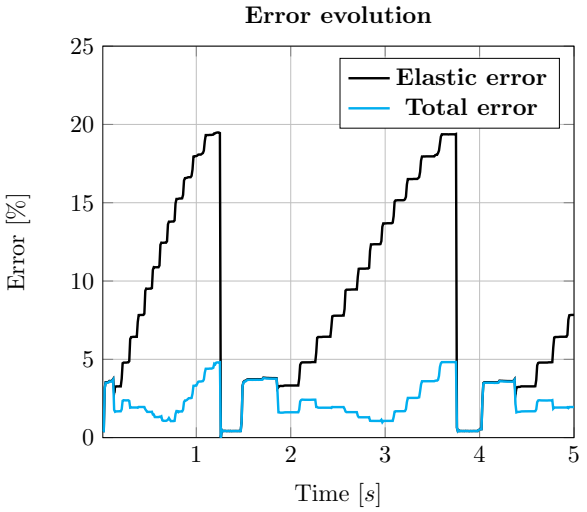

Figure 9: Error evolution introduced by the approximation during a proportional fretting cycle.

It is worth noting that the maximum value of the error is stable regardless of the direction of the tangential proportional loading (Fig. 10) and remains low for non-proportional loading (Fig. 11).

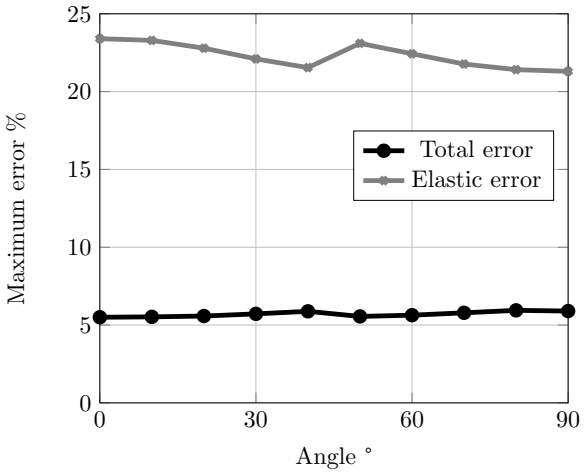

Figure 10: Influence of the loading direction on the maximum error during a proportional fretting cycle.

This approximation of $\underline{v}$ presented is well suited for complex loadings. The spatial reference fields

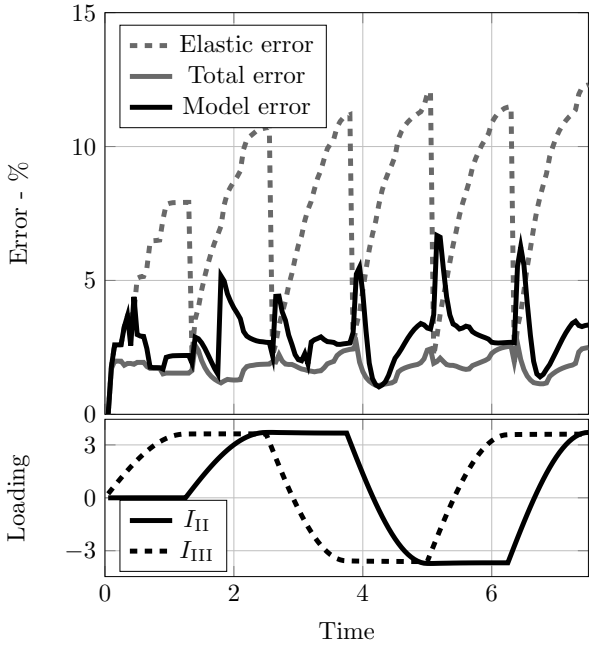

Figure 11: Error evolution introduced by the approximation during a non-proportional fretting cycle (square).

depend exclusively on the local geometry and are suitable for all types of complex loadings.

2.5. Perspective

The evolution the non-linear intensity factors compared to the linear ones shows a curve analogous to a stress-strain curve observed in plasticity (Fig. 12). Moreover, simulation shows (Fig. 13),

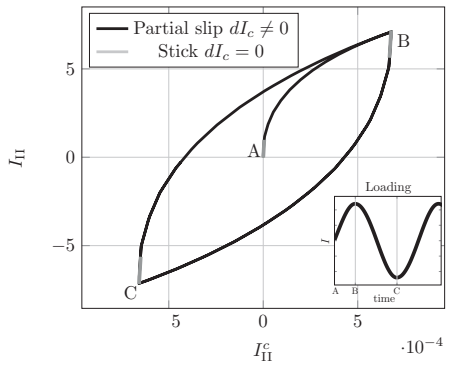

Figure 12: Evolution of the intensity factors during a fretting cycle.

that different loading paths with the same loading amplitude in terms of intensity factors $\underline{I}$ produce a very different response in terms of partial slip.

Both the sliding direction and its intensity $\underline{I}^c$ are path dependent.

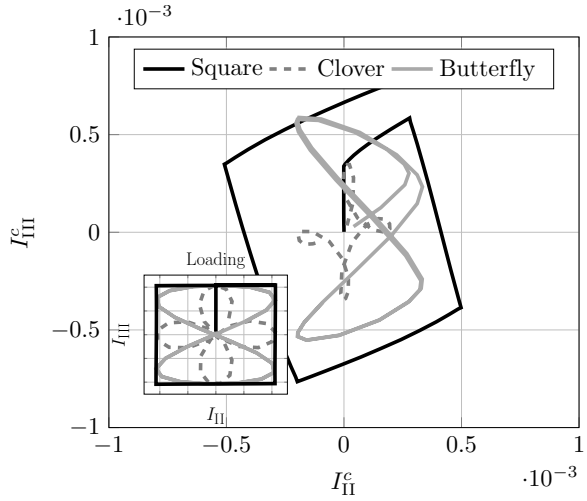

Figure 13: Influence of the loading path.

The linear intensity factors are directly linked to the macroscopic loading so, they can be computed with a coarse mesh FE simulation. The prediction of the non-linear intensity factors (which needs fine mesh) thanks to the linear ones leads to a good approximation of the velocity field close to the contact edge even with rough mesh making this procedure interesting for industrial simulations.

3. Incremental model

The prediction of the non-linear intensity factor $\underline{I}^c$ will be made through an incremental approach to be easy to use for complex loading (variable amplitude, non-proportional). The first step is determining the yield surface which represents the boundary between the stick and partial slip domain.

3.1. Observations

When the loading remains inside the yield surface, all the contact is stuck. Consequently, $\dot{\underline{I}}^c$ is equal to zero and the two errors defined in section 2.4 are equal. Once partial slip happens, the two errors will diverge and will allow to set up a criterion for determining the yield surface boundary:

$$\xi_{el} - \xi_{tot} = 1\% \tag{10}$$

To identify the size and the shape of the yield surface, three steps will be done:

- an initial loading to have partial slip;
- a small unloading to go back to a full elastic behavior and have all the contact stick;
- a final loading to determine the value of $\underline{I}$ when partial slip happens in the direction considered.

Fig. 14 shows the different directions considered and the ellipse obtained. The repetition of the procedure for different initial loadings show the evolution of the yield surface (Fig. 15). It is worth noting that the size of the surface remains constant whereas its center move. By analogy with the plasticity, a kinematic hardening is present.

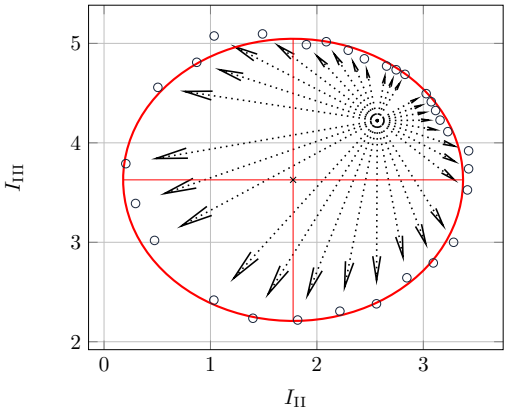

Figure 14: Shape of the stick domain.

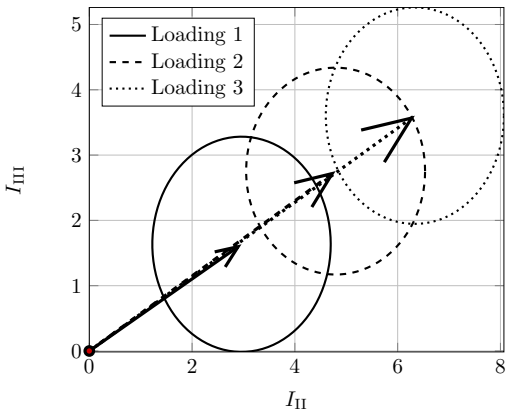

Figure 15: Evolution of the stick domain.

Concerning the sliding direction, Fig. 16 shows three particular directions : the normal to surface, the loading and the sliding direction (which is characterized by $\mathrm{d}I^c$, analogous to the plastic flow) as

function of the loading direction. It is important to notice that the sliding do not appear in the same direction as the loading but it seems linked to the normal of the yield surface. By analogy with the plasticity, a normal plastic flow is present.

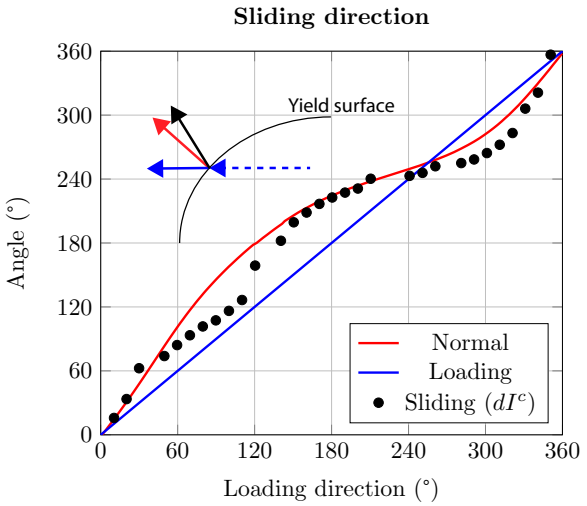

Figure 16: Sliding direction.

3.2. Modeling

To model this non-linear behavior, a bilinear kinematic hardening law is chosen to provide a simple model along with a good precision. At first approximation, the yield surface identify above will be considered circular.

A first yield surface is defined to determine the transition between stick and partial slip:

$$f_1 = \left|\left|\underline{I} - \underline{I}_1^X\right|\right| - \underline{I}_{y_1} \leq 0 \tag{11}$$

A second is defined ($\underline{I}_{y_1} < \underline{I}_{y_2}$) to have a better prediction for the high tangential amplitude:

$$f_2 = \left|\left|\underline{I} - \underline{I}_2^X\right|\right| - \underline{I}_{y_2} \leq 0 \tag{12}$$

When $f_1 < 0$ all the contact is stick, $\mathrm{d}\underline{I}^c = 0$.

If $f_1 = 0$, partial slip happens. The total sliding is defined by two terms, one for each surface:

$$\mathrm{d}\underline{I}^{c\,model} = \mathrm{d}\underline{I}_1^c + \mathrm{d}\underline{I}_2^c \tag{13}$$

The first sliding rate with the direction normal to the yield surface is equal to:

$$\mathrm{d}\underline{I}_1^c = \dot{\lambda}_1 \underline{n}_1 \quad \text{with} \quad \underline{n}_1 = \frac{\partial f_1}{\partial \underline{I}} \tag{14}$$

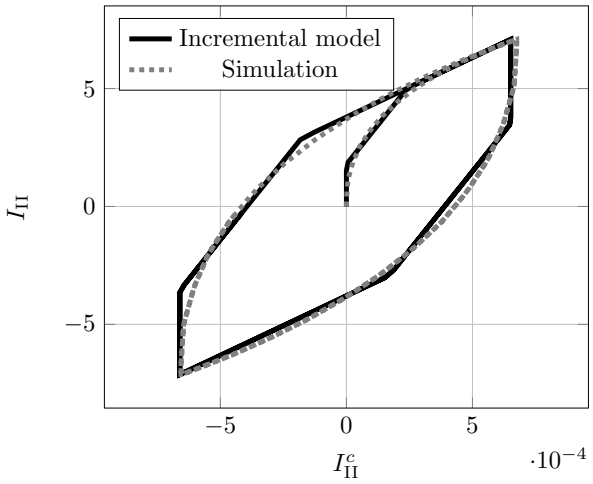

Figure 17: Sliding prediction during a proportional fretting cycle.

And the displacement of the first yield surface center is defined:

$$\mathrm{d}\underline{I}_1^X = \underline{H}_1 \cdot \underline{I}_1^c \tag{15}$$

To avoid interpenetration between the two surfaces, a second sliding rate is specified with a flow vector normal to the surface at the contact point.

$$\mathrm{d}\underline{I}_2^c = \dot{\lambda}_2 \underline{n}_{contact} \tag{16}$$

And the displacement of the second yield surface center is defined:

$$\mathrm{d}\underline{I}_2^X = \underline{H}_2 \cdot \underline{I}_2^c \tag{17}$$

3.3. Error estimation

The hardening coefficients $\underline{H}_*$ and the surface radius I_{y*} are fit by the gradient descent method to minimize the error on a constant amplitude simulation. It is good to notice the value of I_{y1} found with the optimization process is close to the one obtained with the simulation using the partial slip criteria (Eq. 10). The model is able to predict the evolution of $\underline{I}^c$ during a fretting cycle with a proportional tangential loading (Fig. 17).

To estimate more precisely the error, the complementary velocity field $\underline{v}_c^{model}$ predicted by the model (Eq. 18) and the error associated (Eq. 19) are defined.

$$\underline{v}_c^{model} = \dot{I}_{\mathrm{II}}^{c\,model}(t)\underline{\phi}_{\mathrm{II}}^c(\underline{P}) + \dot{I}_{\mathrm{III}}^{c\,model}(t)\underline{\phi}_{\mathrm{III}}^c \tag{18}$$

$$\xi_{model} = \frac{\sqrt{\int_\Omega (\underline{v} - \underline{v}_e - \underline{v}_c^{model})^2}}{\sqrt{\int_\Omega (\underline{v})^2}} \qquad (19)$$

3.3.1. Variable loading amplitude

During a cycle with variable amplitude, the model gives similar result to the simulation (Fig. 18.a). Thanks to the second surface (Eq. 12), the model is able to describe precisely the low and high amplitudes. With regard to the error on the velocity field (Fig. 19), it appears that the complementary field predicted by the model permit to reduce the error, not as much as the complementary field issue from the simulation but to a reasonable level.

3.3.2. Non proportional loading

Concerning non-proportional loadings, the amplitudes predicted are overestimated but the sliding direction is coherent (Fig. 20). Moreover, the total error on the velocity field remains low (Fig. 11) and influence of the loading path on the sliding, observed by the simulations, is well described (Fig. 13).

4. Friction effect

The model presented above works for a constant normal load, complex tangential amplitude and a constant Coulomb coefficient. However, in contact fatigue, surface are damaged because of the friction. Consequently, the Coulomb coefficient evolves during a fretting-fatigue test. In this part, the influence on the model of the non-local Coulomb coefficient [12] (which is directly proportional to the local coefficient) will be studied.

4.1. Stick domain evolution

The Coulomb law determines the limit between stick and slip conditions, hence the evolution of the yield surface in function of Coulomb coefficient is shown in Fig. 21. The size of the stick contact surface is determined by two methods: (i) by simulation using the protocol presented in the section 3.1; (ii) by optimization procedure using gradient descent method to minimize the error.

It is worth noticing that the evolution of the surface radius versus the non-local Coulomb coefficient is linear and directly proportional to its variation.

4.2. Model evolution

Using the same hardening coefficients $\underline{H}_*$ (identified with a Coulomb coefficient $\mu = 0.8$) and the same ratio between the two yield surfaces $\underline{I}_{y_1}/\underline{I}_{y_2}$, Fig. 18 shows that a modification of the non-local Coulomb coefficient can be taken into account only with a variation of the yield surface radius. Moreover, if there are some difference between model and simulation (Fig. 18.c), the error on the total field remains low (Fig. 22).

5. Discussion and conclusion

A novel approach to predict the local velocity field of a fretting case, based on a fracture mechanic analogy, has been shown. Once the reference field is identified for a specific geometry, it is possible to predict the velocity field close to the contact edge thanks to the non-local intensity factors using only the macroscopic loadings. The geometric and gradient effects are included in the reference fields so the use of criteria and laws based on non-local intensity factors are not geometry dependent. Consequently, they can be identified on laboratory tests and easily transferred to industrial structure.

The future works will focus on coupling the non-local description of the velocity field with crack initiation and propagation criteria. The intensity factors will be used as input for the criterion in order to predict when initiation and propagation occur for complex and non-proportional loadings. Moreover, the displacement of the contact edge and the damage accumulation should be taken into account to study normal load variations and all kinds of complex loadings. To complete this work, fretting tests under non-proportional and variable amplitude loadings could be performed to validate results obtained by simulation.

Friction can also be a way of improvement. Indeed, only a Coulomb law with a constant coefficient is considered. However, in contact fatigue, surface will be damaged. Consequently the Coulomb coefficient can evolve over the cycles. Moreover, under partial slip condition, the damage is very localized in the slip zone hence the Coulomb coefficient is not only time dependent but also space dependent. To be more precise concerning the friction, a Coulomb coefficient space and time dependent should be used. However, it can be also interesting to investigate different friction laws dedicate to fretting problem to study how the law can be

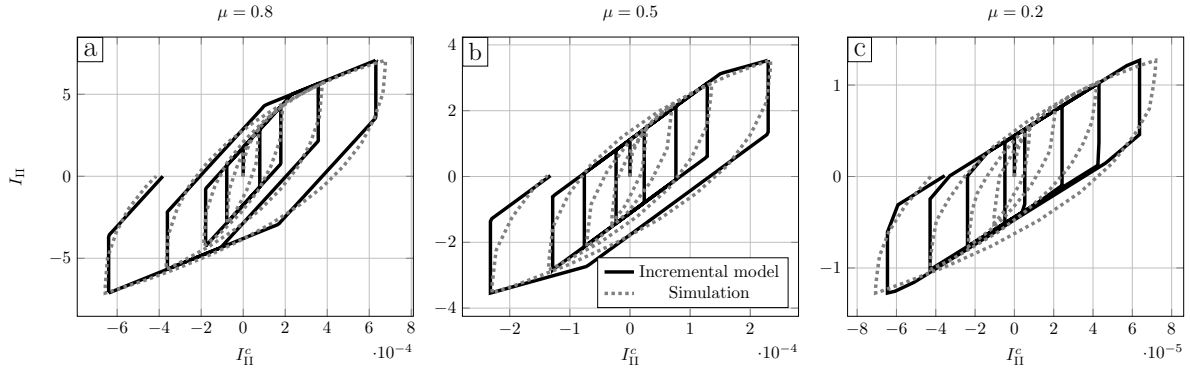

Figure 18: Sliding prediction during proportional fretting cycles.

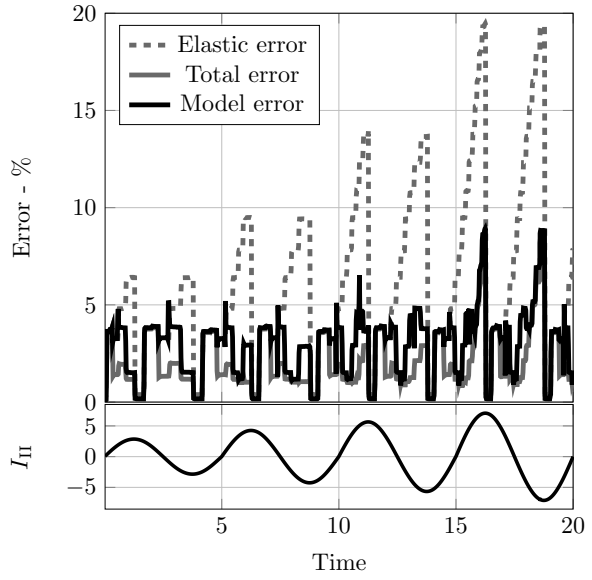

Figure 19: Error evolution with variable tangential loading ($\mu = 0.8$)

translated in terms of non-local quantities and how our model can be modified.

Acknowledgements

The authors are grateful to Safran Aircraft Engines (Safran group) for its financial support, within the IRG COGNAC project framework.

[1] Amargier, R., S. Fouvry, L. Chambon, C. Schwob, and C. Poupon (2010). Stress gradient effect on crack initiation in fretting using a multiaxial fatigue framework. International Journal of Fatigue 32(12), 1904–1912.

[2] Araújo, J. A., L. Susmel, D. Taylor, J. C. Ferro, and E. N. Mamiya (2007). On the use of the Theory of Critical Distances and the Modified Wöhler Curve Method to estimate fretting fatigue strength of cylindrical contacts. International Journal of Fatigue 29(1), 95–107.

[3] Castro, F. C., J. A. Araújo, and N. Zouain (2009). On the application of multiaxial high-cycle fatigue criteria using the theory of critical distances. Engineering Fracture Mechanics 76(4), 512–524.

[4] Ferre, R., S. Fouvry, B. Berthel, and J. A. Ruiz-Sabariego (2013, sep). Stress gradient effect on the crack nucleation process of a Ti-6Al-4V titanium alloy under fretting loading: Comparison between non-local fatigue approaches. International Journal of Fatigue 54, 56–67.

[5] Ferry, B., J. A. Araújo, S. Pommier, and K. Demmou (2017). Life of a Ti–6Al–4V alloy under fretting fatigue: Study of new nonlocal parameters. Tribology International 108(July 2016), 23–31.

[6] Fouvry, S., H. Gallien, and B. Berthel (2014, may). From uni- to multi-axial fretting-fatigue crack nucleation: Development of a stress-gradient-dependent critical distance approach. International Journal of Fatigue 62, 194–209.

[7] Giannakopoulos, A., T. Lindley, and S. Suresh (1998). Aspects of equivalence between contact mechanics and fracture mechanics: theoretical connections and a life-prediction methodology for fretting-fatigue. Acta Materialia 46(9), 2955–2968.

[8] Giannakopoulos, A. E., T. C. Lindley, S. Suresh, and C. Chenut (2000). Similarities of stress concentrations in contact at round punches and fatigue at notches: Implications to fretting fatigue crack initiation. Fatigue and Fracture of Engineering Materials and Structures 23(7), 561–571.

[9] Hills, D. A., A. Thaitirarot, J. R. Barber, and D. Dini (2012). Correlation of fretting fatigue experimental results using an asymptotic approach. International Journal of Fatigue 43, 62–75.

[10] Lindley, T. C. (1997). Fretting fatigue in engineering alloys. Int. J. Fatigue 19(1), 39–49.

[11] Loève, M. (1977). Probability Theory I. 45, 1–10.

[12] Montebello, C. (2015). Analysis of the stress gradient effect in Fretting-Fatigue through a descript Theses, Universit{é} Paris-Saclay.

[13] Montebello, C., S. Pommier, K. Demmou, J. Leroux, and J. Meriaux (2016, jan). Analysis of the stress gradient effect in fretting-fatigue through nonlocal intensity factors. In International Journal of Fatigue, Volume 82, pp. 188–198. Elsevier Ltd.

[14] Papanikos, P. and S. A. Meguid (1994). Theoretical and

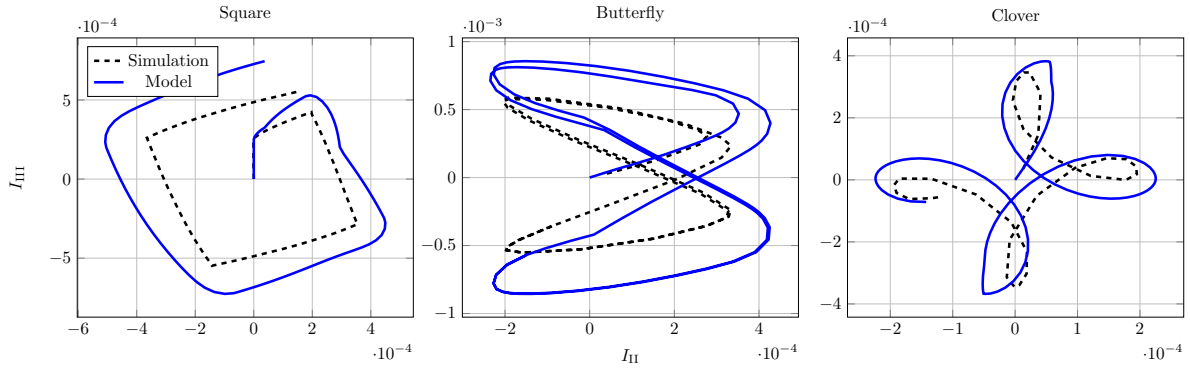

Figure 20: Influence of the loading path.

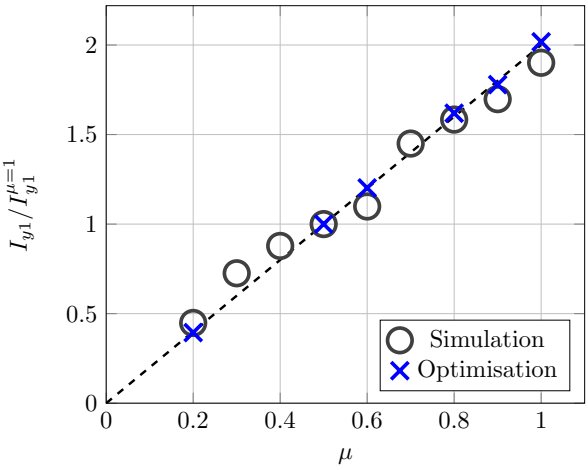

Figure 21: Size evolution of the stick domain.

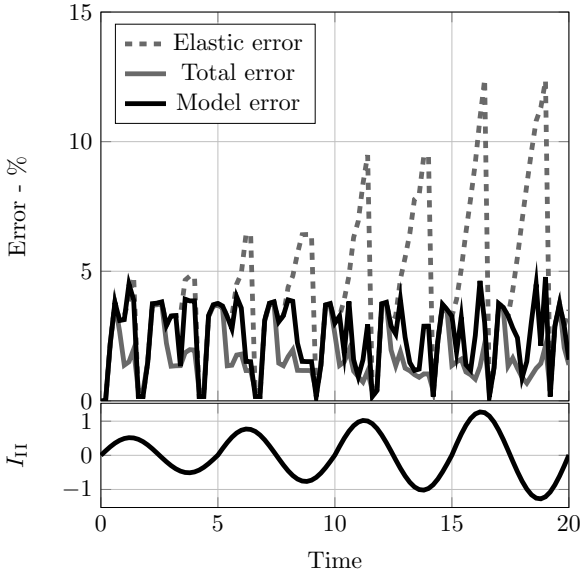

Figure 22: Error evolution with variable tangential loading ($\mu = 0.2$)

Experimental Studies of Fretting-Initiated Fatigue Failure of Aeroengine Compressor Discs. Fatigue & Fracture of Engineering Materials & Structures 17(5), 539–550.

[15] Pommier, S. and R. Hamam (2007). Incremental model for fatigue crack growth based on a displacement partitioning hypothesis of mode I elastic-plastic displacement fields. Fatigue and Fracture of Engineering Materials and Structures 30(7), 582–598.

[16] POMMIER, S., P. LOPEZ-CRESPO, and P. Y. DECREUSE (2009, nov). A multi-scale approach to condense the cyclic elastic-plastic behaviour of the crack tip region into an extended constitutive model. Fatigue & Fracture of Engineering Materials & Structures 32(11), 899–915.

[17] Susmel, L. and D. Taylor (2008, dec). The modified Wöhler curve method applied along with the theory of critical distances to estimate finite life of notched components subjected to complex multiaxial loading paths. Fatigue and Fracture of Engineering Materials and Structures 31(12), 1047–1064.

[18] Taylor, D. (2008). The Theory of Critical Distances: Basics. Engineering Fracture Mechanics 75(7), 1696–1705.

[19] Westergaard, H. M. (1939). Bearing pressures and cracks.